Phase-gradient microscopy in thick tissue with oblique back-illumination

Tim N Ford, Kengyeh K Chu & Jerome Mertz

Phase-contrast techniques, such as differential interference contrast microscopy, are widely used to obtain morphological images of unstained biological samples. The transillumination geometry required for these techniques restricts their application to thin samples. We introduce oblique back-illumination microscopy, a method of collecting *en face* phase-gradient images of thick scattering samples, enabling near-video-rate *in vivo* phase imaging with a miniaturized probe suitable for endoscopy.

Phase-contrast microscopy techniques are widely used in biological research because they can provide high-resolution images of unlabeled samples even when the samples are nearly transparent. For example, differential interference contrast (DIC), which reveals lateral phase gradients, is a popular technique because it provides apparent three-dimensional sample relief through a standard wide-field microscope equipped with a lamp and camera[1]. Simpler techniques based on oblique illumination can also be used with wide-field microscopes, and they provide similar imaging to DIC[2–5]. However, these techniques must be operated in transillumination configurations to reveal lateral phase gradients, limiting their use to thin samples. Because it is sometimes necessary to work with thick samples (for example, in endoscopy or *in vivo* applications), there is a need for a method that can provide DIC-like imaging in thick samples. We introduce such a method here.

Our technique is called oblique back-illumination microscopy (OBM). As its name suggests, this technique is similar in principle to oblique illumination microscopy, with the notable difference that the illumination source and detection optics reside on the same side of the sample (that is, in a reflection geometry), allowing OBM to be used on samples of any thickness. Unlabeled samples can, of course, be imaged with microscopes that use direct light reflection. The most successful of these for tissue imaging is optical coherence tomography, which, like OBM, can also be used in a wide-field *en face* configuration[6]. However, microscopes based on light reflection intrinsically reveal only sample structures that vary rapidly in the axial direction, such as sharp interfaces or particles much smaller than the illumination wavelength[7]. In contrast, microscopes based on light

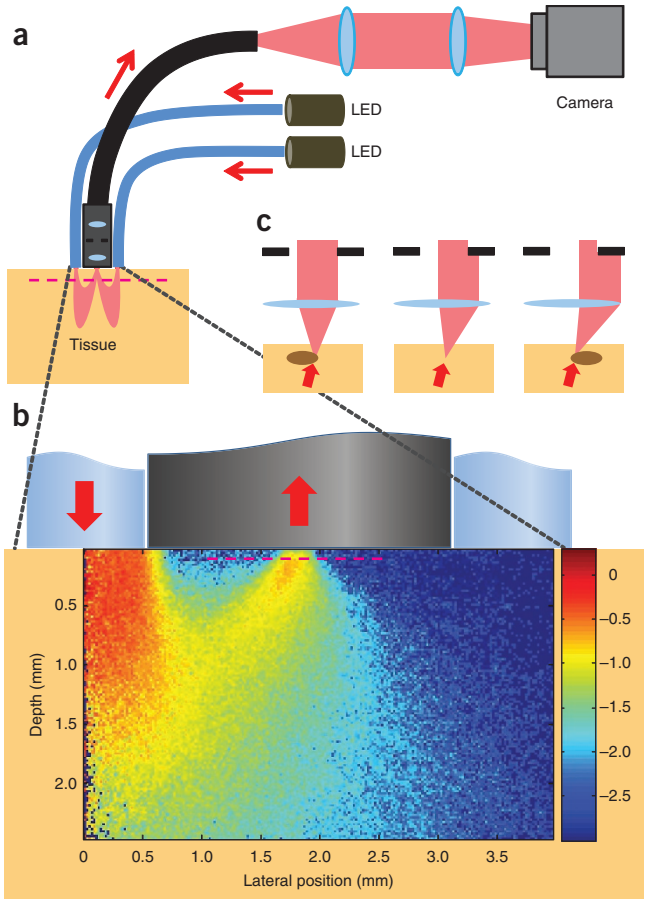

Figure 1 | An OBM setup with a contact-mode endomicroscope probe. (**a**) Illumination from two LEDs is sequentially delivered to a thick sample by diametrically opposed optical fibers attached to the probe housing. Multiple scattering in the sample redirects the light so that it transilluminates the focal plane of the probe micro-objective (magenta dashed line). An image from the focal plane is then relayed by a flexible fiber bundle to a digital camera. (**b**) Close-up of the probe distal end, onto which is superposed a density map obtained by Monte Carlo simulation of the light energy in the sample that was injected by a single fiber (from left) and collected by the micro-objective (Online Methods). Note the obliquity of the light distribution through the focal plane. (**c**) Oblique transillumination leads to phase-gradient contrast. With no phase gradient, oblique illumination is partially blocked by the aperture in the micro-objective (center). Phase gradients caused by variations in the index of refraction at the focal plane tilt the light more or less (right or left) depending on the slope of the variation. As a result, more or less light is blocked by the micro-objective aperture, leading to intensity variations in the recorded image and hence phase-gradient contrast[4,5].

Department of Biomedical Engineering, Boston University, Boston, Massachusetts, USA. Correspondence should be addressed to J.M. (jmertz@bu.edu).

RECEIVED 20 APRIL; ACCEPTED 6 SEPTEMBER; PUBLISHED ONLINE 28 OCTOBER 2012; DOI:10.1038/NMETH.2219

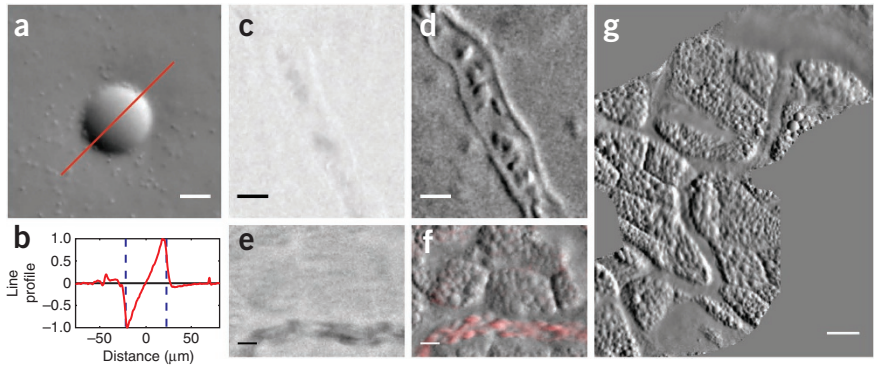

Figure 2 | Demonstration of OBM in a tissue phantom and *in vivo*. (**a**) Phase-gradient image of a 45-μm polystyrene bead in scattering medium (2-μm beads in agarose, **Supplementary Video 1**). Note that 2-μm beads are readily visible. (**b**) Phase-gradient profile corresponding to **a**. (**c**–**f**) Simultaneously acquired absorption (**c**,**e**) and phase-gradient (**d**,**f**) images of the CAM vascular system of a chicken embryo (day 11) *in ovo*. Individual red blood cells (RBCs) and vessel walls are clearly visible (**Supplementary Video 2**). (**f**) Moving RBCs are highlighted in red using a sliding three-frame temporal variance filter (**Supplementary Video 3**). (**g**) A CAM vasculature mosaic reconstructed from **Supplementary Videos 4** and **5**. Scale bars, 20 μm (**a**,**c**–**f**) and 50 μm (**g**).

transmission do not have this constraint and can reveal sample structure even slowly varying in the lateral direction, providing images of subtle sample features impossible to see in reflection mode. Notably, although OBM is configured in a reflection geometry, it is a 'transmission microscope in disguise'. In effect, OBM uses multiple scattering in tissue to convert epi-illumination into transillumination. Because the illumination source is offset from the optical detection axis, the transillumination is oblique (**Fig. 1**), which leads directly to phase-gradient contrast. However, image intensity is also influenced by sample absorption. The use of two diametrically opposed off-axis sources permits the acquisition of two raw images with similar values for absorption contrast but with opposing values for phase-gradient contrast (**Supplementary Fig. 1**). The subtraction of these raw images enhances phase-gradient contrast while canceling absorption contrast; addition of the raw images has the opposite effect, revealing only absorption contrast while canceling phase-gradient contrast. By this method, the sequential acquisition of two raw images using alternating illumination sources decouples absorption and phase-gradient contrast[5].

We present results from a miniaturized OBM that we built using a flexible endomicroscope probe comprising a distal micro-objective attached to an imaging fiber bundle (Online Methods). Two optical fibers attached on opposite sides of the micro-objective housing deliver light from two independently controlled LEDs to the sample. The endomicroscope probe was designed to operate in contact mode, which means that the micro-objective does not collect light reflected directly from the sample surface. Instead, the micro-objective collects only light that has been multiply scattered in the sample and redirected upward through the focal plane, located in this case at a depth of 60 μm (the working distance of the micro-objective). Unless stated otherwise, all images presented here are individual frames from movies that we acquired, processed and displayed at a net rate of 17.5 Hz using a double-shutter camera that reads images pairwise. The exposure time per raw image was typically 1–5 ms.

We first used OBM to image a 45-μm polystyrene bead embedded in a scattering tissue phantom consisting of 2-μm beads in agarose (**Fig. 2a**). The phase gradient induced by the bead was observed to be approximately linear (**Fig. 2b**). Because the phase-gradient image was derived from a difference of raw images, it contains

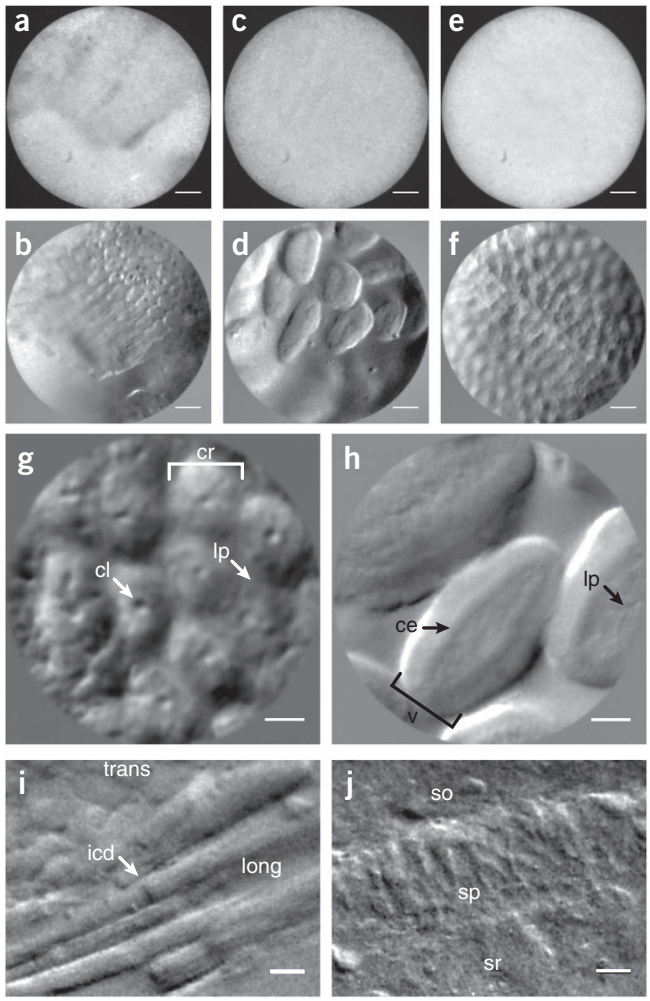

Figure 3 | Demonstration of OBM in excised mouse tissue. (**a**–**f**) Simultaneously acquired amplitude (**a**,**c**,**e**) and phase-gradient (**b**,**d**,**f**) images of intestinal epithelium taken with a 1× micro-objective (600-μm field of view (FOV)). (**g**,**h**) Higher-magnification phase-gradient images of the epithelium in the distal colon (**g**) and small intestine (**h**), captured with a 2.5× micro-objective (240-μm FOV). Crypts of Lieberkühn (cr), crypt lumens (cl) and lamina propia (lp) are indicated with white arrows (**g**, **Supplementary Video 6**); ileal villi (v), columnar epithelium (ce) and lamina propia are indicated with black arrows (**h**, **Supplementary Video 7**). (**i**) Transverse (trans) and longitudinal (long) aspects of mouse cardiac muscle tissue. Intercalated discs (icd) are readily distinguishable. (**j**) Pyramidal neurons in the CA1 region of mouse hippocampus. (**Supplementary Video 8**). Stratum oriens (so), stratum pyramidale (sp) and stratum radiatum (sr) are apparent. Scale bars, 75 μm (**a**–**f**), 30 μm (**g**,**h**) and 20 μm (**i**,**j**).

both positive and negative values (in all our phase gradient images, the 0 value is represented as a medium gray). Because phase gradients must, by definition, arise from apparent sample structure, they must also arise from the vicinity of the focal plane (objects out of focus are blurred and show little structure). Thus, phase-gradient imaging shows apparent out-of-focus background rejection. This is demonstrated in **Supplementary Video 1**, in which only the 2-μm beads in focus are visible. An axial profile of these beads shows a full width–half maximum axial resolution of 6 μm (**Supplementary Fig. 2**).

We performed simultaneous absorption and phase-gradient imaging of the chorioallantoic membrane (CAM) *in vivo* in a day 11 chicken embryo (**Fig. 2c–g** and **Supplementary Videos 2–5**). The absorption images had low contrast compared to the phase-gradient images (**Supplementary Video 4**). Because the absorption images were derived from the sum of raw images, their values are positive definite (values of 0 are shown in black), and they do not show out-of-focus background rejection (such imaging is similar to orthogonal polarization spectral imaging)[8]. Compared to images obtained from optical coherence tomography, OBM images are free of speckles. Moreover, owing to the large photon fluxes involved, OBM images are relatively free of shot noise. Intensity noise arose, in our case, mostly from inhomogeneous image sampling caused by an uneven distribution of fiber cores in the imaging fiber bundle (Online Methods).

Our endomicroscope probe was designed for gastrointestinal imaging. Accordingly, we performed simultaneous absorption and phase-gradient imaging of excised, unstained mouse intestinal epithelium (**Fig. 3a–h**). The absorption images are essentially featureless, whereas the phase-gradient images are information rich. For example, crypts of Lieberkühn and ileal villi are readily visible (**Fig. 3g**,**h** and **Supplementary Videos 6** and **7**), illustrating a potential use for OBM in *in situ* histopathology and 'optical biopsies'.

Finally, we imaged other types of tissue, such as mouse cardiac muscle and brain tissue (**Fig. 3i**,**j** and **Supplementary Video 8**). These images were similar in appearance to images obtained by DIC but were acquired from tissue sections many millimeters thick. Again, our imaging depth was limited by the 60-μm working distance of our micro-objective. Somewhat deeper imaging can be achieved with an objective with a longer working distance, which we demonstrated using a standard microscope setup (**Supplementary Figs. 3** and **4**).

In summary, we have presented an apparatus that, to our knowledge, is the first to provide sub-surface, DIC-like (that is, transmission-like) phase-gradient imaging from thick scattering tissue in a wide-field reflection geometry. The apparatus is simple, fast, robust and inexpensive, making it broadly useful to biological and clinical researchers alike.

METHODS

Methods and any associated references are available in the online version of the paper.

Note: Supplementary information is available in the online version of the paper.

ACKNOWLEDGMENTS

We thank S. Singh (Boston University) and J. Ritt (Boston University) for supplying mouse gastrointestinal tissue samples; M. Baum (Boston University) for supplying skin and brain tissue samples; K. Calabro (Boston University) for helping develop the Monte Carlo simulation code; R. Wu (Boston University) for help with building the microscope setup used for **Supplementary Figures 3** and **4**; and all the members of the Biomicroscopy Lab for their helpful conversations and careful review of this manuscript. This work was supported by a US National Institutes of Health grant R01-EB010059 (T.N.F., K.K.C. and J.M.).

AUTHOR CONTRIBUTIONS

T.N.F., K.K.C. and J.M. conceived and developed the technique. T.N.F. built the setup and acquired the data. T.N.F. and J.M. wrote the manuscript. J.M. supervised the project.

COMPETING FINANCIAL INTERESTS

The authors declare no competing financial interests.

Published online at http://www.nature.com/doifinder/10.1038/nmeth.2219. Reprints and permissions information is available online at http://www.nature.com/reprints/index.html.

1. Nomarski, G. *J. Phys. Radium* **16**, S9–S13 (1955).
2. Saylor, C.F. *J. Res. Natl. Bur. Stand. (US)* **15**, 277 (1935).
3. Axelrod, D. *Cell Biophys.* **3**, 167–173 (1981).
4. Yi, R., Chu, K.K. & Mertz, J. *Opt. Express* **14**, 5191–5200 (2006).
5. Mehta, S.B. & Sheppard, C.J.R. *Opt. Lett.* **34**, 1924–1926 (2009).
6. Dubois, A. & Boccara, A.C. in *Optical Coherence Tomography* (eds. Drexler, W. & Fujimoto, J.G.) Ch. 19, 565–591 (Springer, 2009).
7. Mertz, J. *Introduction to Optical Microscopy* (Roberts & Company, 2009).
8. Groner, W. *et al. Nat. Med.* **5**, 1209–1212 (1999).

ONLINE METHODS

Hardware setup. Aspheric condenser lenses (Thorlabs ACL5040-A) coupled white light from two LEDs (Luxeon Star MR-WC310-20s) into optical fibers (Thorlabs BFL48-1000; 0.48 numerical aperture (NA); 1,000-μm core). The fibers launched the illumination into the sample (25 mW per channel at the fiber output), where multiple scattering redirected it through the focal plane and into a micro-objective (Mauna-Kea Technologies; 2.6 mm diameter; 1× or 2.5× magnification; 60-μm working distance; water immersion; 0.8 NA) coupled to an imaging fiber bundle (30,000 cores; 600-μm active area). The separation distance between the fiber axis and the micro-objective probe axis was ~1.8 mm. Standard microscope optics (Olympus Plan 10× 0.25 NA air objective, Linos AC f = 200 mm tube lens; 4f configuration) imaged the proximal face of the fiber bundle onto a digital camera (PCO Pixelfly USB; 14-bit; 2 × 2 binning; 35 frames per second (f.p.s.); 1- to 5-ms exposure time per illumination direction), which recorded the images. Motion artifacts were minimized by operating the camera in double-shutter mode, which reduced the interframe delay between exposures (200 μs)[9]. Illumination power delivered by the left and right optical fibers was triggered to overlap with the first and second frame in the each image pair, respectively. Camera readout time limited the frame rate. In a separate experiment, an epi-illumination path was added to compare OBM with traditional reflection imaging. The strong specular reflection from the proximal fiber bundle surface was largely rejected by using a polarizing beam splitter (**Supplementary Fig. 5**). Custom-written software (National Instruments LabVIEW 11.0) performed the image acquisition and display. A data acquisition card (National Instruments PCI-6221) synchronized illumination gating and camera exposure.

Image processing. A preprocessing routine described previously[9] first corrected for the quasiperiodic sampling pattern imparted by the fiber bundle cores. Each raw image was then normalized by its respective low-pass filtered version (Gaussian filter kernel with $\sigma = 80$ pixels) to correct for nonuniform illumination profiles and thus 'flatten' the images. The two normalized images were then added or subtracted to produce absorption-only or phase-gradient-only images, respectively (**Supplementary Fig. 1**). Unless otherwise stated, positive definite absorption images are displayed with a linear grayscale mapping the value 0 to black and the maximum value of the image to white. Phase-gradient images are displayed with a linear grayscale mapping such that 0 is represented by the middle gray level and the image is scaled to fill the dynamic range of the display (**Supplementary Fig. 5**). A graphics-processing unit (GPU, NVIDIA GTX280) running custom-written software written in CUDA-C[10] performed the image processing.

Monte Carlo simulations. We performed simulations using CUDAMCML[11], a modification of MCML[12] enabling execution on GPUs. We further modified CUDAMCML to execute on a cluster of CUDA-enabled workstations[13]. We modeled the tissue with a semi-infinite slab geometry and tissue optical parameters $n_{tissue} = 1.37$, $l_s = 150$ μm, $l_s^* = 3{,}000$ μm and $g = 0.95$ (where n is the index of refraction, l_s and l_s^* are the scattering and transport mean free path lengths, respectively, and the anisotropy factor $g = 1 - l_s / l_s^*$) . Illumination fiber parameters were $n_{fiber} = 1.37$, diameter = 1,000 μm and numerical aperture (NA) = 0.48. Micro-objective probe parameters were $n_{probe} = 1.37$, diameter = 240 μm and NA = 0.8. Fiber-probe separation distance (d) was 1,818 μm. A Henyey-Greenstein phase function characterized photon scattering events[14]. We simulated 10^5 photons to estimate photon path density as a function of lateral position and depth, revealing the 'photon banana' (displayed in arbitrary units in log scale, **Fig. 1b**). We simulated 10^8 photons to estimate the distribution of exit angles of the detected photons as a function of fiber-probe separation (**Supplementary Figs. 6** and **7**).

Tissue phantom preparation. We prepared the scattering tissue phantom by heating a 30-ml solution of 2% (w/v) agarose (Sigma A5093-100G), 5% 2-μm diameter polystyrene beads (Polysciences 19814-15) and 0.1% 45-μm diameter polystyrene beads (Polysciences 07314-5) in H_2O to 75 °C on a hot plate and then pouring the mixture into a 60 mm × 15 mm cell culture dish (Corning 430166). We covered the phantom with paraffin film and left it to cool to room temperature before imaging. Mie theory estimated the optical properties of the bulk medium to be $l_s = 74$ μm, $l_s^* = 1{,}040$ μm and $g = 0.93$. The indices of refraction of hydrated agarose gel and polystyrene beads were $n = 1.35$ and $n = 1.59$, respectively[15]. We performed the imaging through water.

Chicken embryo preparation. Fertilized *Gallus gallus* eggs (Carolina Biological Supply Co. 139290) were stored in an incubator at 37 °C and 50% humidity, being turned every 7 h to prevent fusion of the chorioallantoic membrane (CAM) with the shell membrane. Imaging was performed at embryonic day 11. A 1-cm diameter region of the shell and shell membrane was removed exposing the embryo and CAM. A layer of 37 °C saline was dripped over the preparation before imaging *in ovo* with the OBM probe. Following imaging, the embryos were euthanized by hypothermia by storing the eggs at –15 °C.

Mouse tissue preparation. *Gastrointestinal tissue:* 6-week-old C57BL/6 mice were euthanized by CO_2 inhalation, and the gastrointestinal tracts were immediately excised and washed with 4% paraformaldehyde. The colon and small intestine were cut longitudinally, unrolled and cleared of fecal matter. The preparations were incubated in 4% paraformaldehyde for 72 h. Before *ex vivo* imaging, the tissues were pinned to a silicone elastomer slab (Sylgard 184, Corning) to expose the apical surfaces. Residual mucus and fecal matter were gently washed away with saline before imaging. *Cardiac tissue:* The intact heart was removed from the same mice as above and incubated in 4% paraformaldehyde for 72 h. Upon *ex vivo* imaging, a transverse cut exposing the left ventricular cavity was made, exposing cardiac muscle fibers in both transverse and longitudinal aspects. *Brain tissue:* 8-week-old Swiss Webster mice were anesthetized and decapitated, and the brain was incubated in 30% sucrose for 72 h. A 4.3-mm thick coronal slice was made to expose the CA1 region of the hippocampus. *Skin tissue:* Shaved, 3 cm × 3 cm area sections of ventral skin were removed from the same mice as above and incubated in 4% paraformaldehyde for 24 h. Upon *ex vivo* imaging the tissue was pinned to a silicon elastomer slab. The animals used in this study were treated in accordance with the guidelines of the Institutional Animal Care and Use Committee of Boston University.

doi:10.1038/nmeth.2219

9. Ford, T.N., Lim, D. & Mertz, J. *J. Biomed. Opt.* **17**, 021105 (2012).
10. CUDA C Programming Guide Version 4.2. <http://developer.nvidia.com/cuda/cuda-toolkit> (NVIDIA, 2012).
11. Alerstam, E., Svensson, T. & Andersson-Engels, S. *J. Biomed. Opt.* **13**, 060504 (2008).
12. Wang, L.-H., Jacques, S.L. & Zheng, L.-Q. *Comput. Meth. Prog. Biomed.* **47**, 131–146 (1995).
13. Calabro, K.W., Aizenberg, E. & Bigio, I.J. *Proc. SPIE* **8230**, 82300H (2012).
14. Henyey, L.G. & Greenstein, J.L. *Astrophys. J.* **93**, 70–83 (1941).
15. Pogue, B.W. & Patterson, M.S. *J. Biomed. Opt.* **11**, 041102 (2006).